A STRESS ANALYSIS FOR A COATED FUEL PARTICLE OF A HTGR USING A FINITE ELEMENT METHOD

YOUNG MIN KIM* and MOON SUNG CHO
Korea Atomic Energy Research Institute
1045 Daedeok-daero, Yuseong-gu, Daejeon, 305-353, Korea
*Corresponding author. E-mail : nymkim@kaeri.re.kr

A finite element method utilizing the Galerkin form of the weighted residuals procedure was developed to estimate the mechanical behavior for a coated fuel particle (CFP) of a high temperature gas-cooled reactor (HTGR). Through a weak formulation, finite element equations for multiple layers were set up to calculate the displacements and stresses in a CFP. The finite element method was applied to the stress analyses for three coating layers of a tri-isotropic coated fuel particle (TRISO) of a HTGR. The stresses calculated by the finite element method were in good agreement with those from a previously developed computer code and depicted the typical stress behavior of the coating layers very well. The newly developed finite element method performs a stress analysis for multiple bonded layers in a CFP by changing the material properties at any position in the layers during irradiation.

KEYWORDS : Coated Fuel Particle, Coating Layers, HTGR, Galerkin, Finite Element Method, TRISO

1. INTRODUCTION

The HTGR fuel element called a pebble, or a compact contains a very large number of CFPs in it. During a reactor operation, the CFP generates heat through the fission of nuclear material, accompanying a fission product generation. The CFP should maintain its integrity during its lifetime in order to contain the fission products. However, it is exposed to many harmful thermal, chemical, and mechanical environments in a fuel element which can cause particle failure. The particle failure occurs when the stresses developed in the coating layers of a CFP exceed the strengths of the coating layers. Thus, it is very important to estimate the stress distribution across the coating layers of a CFP during a reactor operation.

Various analytical methods have been developed to calculate the stresses of the coating layers of a CFP [1-5]. In the analytical methods have been solved coupled second-order differential equations for radial displacements or stress components. It has been known that the analytical methods execute very quickly on a computer once their solutions are derived. For that reason, they have been preferred for the time-consuming estimation of the failure probability of a batch of CFPs using a Monte Carlo method. The solution procedures, however, are very complicated, and they must be repeated every time the related boundary conditions are altered. Some numerical analyses using general-purpose finite element software have been applied to the verification of the analytical solutions and the stress analysis for a CFP that is under asymmetrical conditions such as de-bonding, cracking, or asphericity of a coating layer [6-8]. These numerical methods usually require far more time than the analytical solutions when they are applied to the Monte Carlo calculation of the failure probabilities.

The purpose of this study is to develop a stress analysis method for a CFP which can be incorporated into a HTGR fuel performance analysis code written in a programming language. The method should be easily programmed for use on a digital computer and applicable to any deformation models and designs of a CFP. In this study, a finite element method using the Galerkin form of the weighted residuals procedure was selected as the stress analysis method for a CFP. Its solution procedure is very simple and does not need to be repeated every time the number of coating layers changes as compared to the above-mentioned analytical solutions. However, it is expected to be less competitive for the calculation of a failure probability using a Monte Carlo calculation. But the disadvantage is offset by the fact that the calculation of a failure probability can be complemented by relatively less time-consuming alternatives such as a full integration method [9].

2. NUMERICAL MODELING FOR A MECHANICAL ANALYSIS

A TRISO consists of a fuel kernel, a low-density pyrocarbon layer called a buffer, and three coating layers as shown in Fig. 1. The coating layers consist of an inner pyrocarbon (IPyC) layer, a silicon carbide (SiC) layer, and an outer pyrocarbon (OPyC) layer. A gap can be created between two layers due to the de-bonding of two adjacent layers during irradiation. Under fast neutron irradiation, the coating layers experience irradiation-
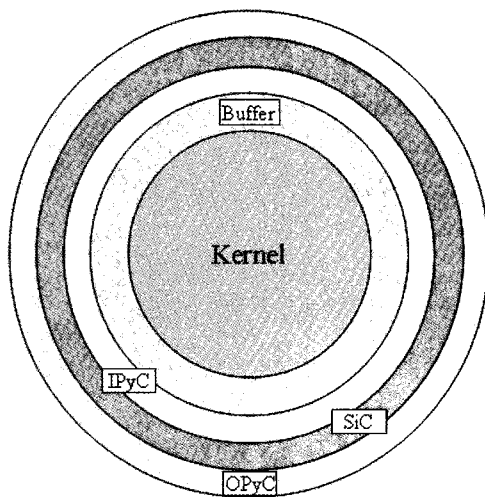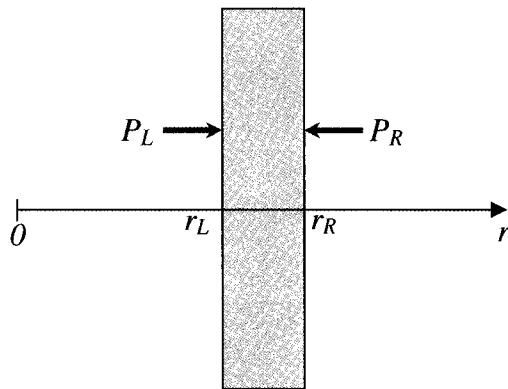

Fig. 1. A Tri-isotropic Coated Fuel Particle

P = pressure (≥ 0)
r = radial coordinate

Fig. 2. A Spherical Shell under Pressure

induced creep and irradiation-induced dimensional change. The gas pressure due to carbon monoxide, carbon dioxide, and fission gases and the contact pressure resulting from 'kernel and coatings mechanical interactions' (KCMIs) are applied to the inner surface of the IPyC layer. An ambient pressure is acting on the outer surface of the OPyC layer by a matrix material surrounding a CFP.

2.1 A spherical Layer

Each coating layer of a TRISO in Fig. 1 can be assumed to be a spherical shell under the pressures at its inner and outer surfaces like in Fig. 2. Under irradiation, the shell is assumed to experience elastic deformation, thermal expansion, irradiation-induced dimensional change, and irradiation-induced creep.

The stress-strain relation for the shell at fluence ϕ can be represented in the following matrix equation.

$$[C]\{\sigma\} = \{\varepsilon\} - \{\varepsilon^{th}\} - \{\varepsilon^{sw}\} - \{\varepsilon^{cr}\}, \tag{1}$$

where

$$\{\sigma\}^T = \{\sigma_r, \sigma_\theta\}, \ \{\varepsilon\}^T = \{\varepsilon_r, \varepsilon_\theta\}, \ \{\varepsilon^{th}\}^T = \{\varepsilon_r^{th}, \varepsilon_\theta^{th}\},$$

$$\{\varepsilon^{sw}\}^T = \{\varepsilon_r^{sw}, \varepsilon_\theta^{sw}\}, \ \{\varepsilon^{cr}\}^T = \{\varepsilon_r^{cr}, \varepsilon_\theta^{cr}\},$$

and the matrix $[C]$ is expresses as follows.

$$[C] = \frac{1}{E}\begin{bmatrix} 1 & -2\nu \\ -\nu & 1-\nu \end{bmatrix}. \tag{2}$$

The creep strain vector of a pyrocarbon is given as follows [10].

$$\{\varepsilon^{cr}\} = \int_0^\phi [A]\{\sigma\} d\tau, \tag{3}$$

where

$$[A] = K\begin{bmatrix} 1 & -2\mu \\ -\mu & 1-\mu \end{bmatrix}. \tag{4}$$

For the spherical shell, the strain-displacement relationship and the equilibrium equation are given respectively by the following two equations [11].

$$\begin{Bmatrix} \varepsilon_r \\ \varepsilon_\theta \end{Bmatrix} = \begin{Bmatrix} \dfrac{\partial u}{\partial r} \\ \dfrac{u}{r} \end{Bmatrix}, \tag{5}$$

$$\frac{\partial \sigma_r}{\partial r} + \frac{2}{r}(\sigma_r - \sigma_\theta) = 0. \tag{6}$$

Differentiating Eq. (1) to (3) with respect to fluence gives

$$\frac{\partial}{\partial \phi}([C]\{\sigma\}) + [A]\{\sigma\} = \frac{\partial}{\partial \phi}(\{\varepsilon\} - \{\varepsilon^{th}\} - \{\varepsilon^{sw}\}). \tag{7}$$

Eq. (7) can be expanded into a finite difference equation over a fluence interval as follows.

$$\{\sigma\}^{(n)} = [G]^{(n)}\left(\{\Delta\varepsilon\}^{(n)} - \{\Delta\varepsilon^{th}\}^{(n)} - \{\Delta\varepsilon^{sw}\}^{(n)}\right) + [B]^{(n)}\{\sigma\}^{(n-1)}, \tag{8}$$

where

$$[G]^{(n)} = ([C]^{(n)} + \beta\Delta\phi^{(n)}[A]^{(n)})^{-1},$$

$$[B]^{(n)} = [G]^{(n)}([C]^{(n-1)} - (1-\beta)\Delta\phi^{(n)}[A]^{(n-1)}),$$

$$\Delta\phi^{(n)} = \phi^{(n)} - \phi^{(n-1)},$$

$$\beta = \begin{cases} 0 & \text{for fully explicit method} \\ 0.5 & \text{for Crank-Nicholson method}, \\ 1 & \text{for fully implicit method} \end{cases}$$

$$\{\Delta\varepsilon\}^{(n)} = \{\varepsilon\}^{(n)} - \{\varepsilon\}^{(n-1)}, \quad \{\Delta\varepsilon^{th}\}^{(n)} = \{\varepsilon^{th}\}^{(n)} - \{\varepsilon^{th}\}^{(n-1)},$$

$$\{\Delta\varepsilon^{sw}\}^{(n)} = \{\varepsilon^{sw}\}^{(n)} - \{\varepsilon^{sw}\}^{(n-1)}.$$

Inserting Eq. (5) into Eq. (8) gives

$$\{\sigma\}^{(n)} = [G]^{(n)}\begin{Bmatrix} \dfrac{\partial u}{\partial r} \\ \dfrac{u}{r} \end{Bmatrix} - [G]^{(n)}\left(\{\varepsilon\}^{(n-1)} + \{\Delta\varepsilon^{th}\}^{(n)} + \{\Delta\varepsilon^{sw}\}^{(n)}\right) + [B]^{(n)}\{\sigma\}^{(n-1)}, \tag{9}$$

where $u = u^{(n)}$ and $r = r^{(n)}$. The partial derivative of radial stress with respect to radial coordinate can be obtained

from Eq. (9).

$$\frac{\partial \sigma_r^{(n)}}{\partial r} = g_{11}\frac{\partial^2 u}{\partial r^2} + \frac{\partial g_{11}}{\partial r}\frac{\partial u}{\partial r} + \frac{g_{12}}{r}\frac{\partial u}{\partial r} - g_{12}\frac{u}{r^2} + \frac{u}{r}\frac{\partial g_{12}}{\partial r}$$
$$+ \sigma_r^{(n-1)}\frac{\partial b_{11}}{\partial r} + b_{11}\frac{\partial \sigma_r^{(n-1)}}{\partial r} + \sigma_\theta^{(n-1)}\frac{\partial b_{12}}{\partial r} + b_{12}\frac{\partial \sigma_\theta^{(n-1)}}{\partial r}$$
$$- g_{11}\frac{\partial}{\partial r}\left(\varepsilon_r^{(n-1)} + \Delta\varepsilon_r^{th,(n)} + \Delta\varepsilon_r^{sw,(n)}\right) - \left(\varepsilon_r^{(n-1)} + \Delta\varepsilon_r^{th,(n)} + \Delta\varepsilon_r^{sw,(n)}\right)\frac{\partial g_{11}}{\partial r}$$
$$- g_{12}\frac{\partial}{\partial r}\left(\varepsilon_\theta^{(n-1)} + \Delta\varepsilon_\theta^{th,(n)} + \Delta\varepsilon_\theta^{sw,(n)}\right) - \left(\varepsilon_\theta^{(n-1)} + \Delta\varepsilon_\theta^{th,(n)} + \Delta\varepsilon_\theta^{sw,(n)}\right)\frac{\partial g_{12}}{\partial r} \tag{10}$$

where the g and b are the elements of the matrices $[G]$ and $[B]$, respectively, and they depend on the Young's modulus, Poisson's ratio, irradiation creep coefficient, Poisson's ratio in irradiation creep, fluence increment, and the β factor. Their mathematical forms appear in Appendix A. Inserting Eq. (10) and the expressions for the radial and tangential stresses in Eq. (9) into the equilibrium equation, Eq. (6), gives the following second-order differential equation.

$$\frac{\partial^2 u}{\partial r^2} + \frac{\zeta_1}{r}\frac{\partial u}{\partial r} + \frac{\zeta_2}{r^2}u = \lambda_1 + \frac{\lambda_2}{r}, \tag{11}$$

where

$$\lambda_1 = \frac{\partial}{\partial r}\left(\varepsilon_r^{(n-1)} + \Delta\varepsilon_r^{th,(n)} + \Delta\varepsilon_r^{sw,(n)}\right) + \zeta_3\frac{\partial}{\partial r}\left(\varepsilon_\theta^{(n-1)} + \Delta\varepsilon_\theta^{th,(n)} + \Delta\varepsilon_\theta^{sw,(n)}\right)$$
$$- \zeta_4\frac{\partial \sigma_r^{(n-1)}}{\partial r} - \zeta_5\frac{\partial \sigma_\theta^{(n-1)}}{\partial r},$$

$$\lambda_2 = \zeta_6\left(\varepsilon_r^{(n-1)} + \Delta\varepsilon_r^{th,(n)} + \Delta\varepsilon_r^{sw,(n)}\right) + \zeta_7\left(\varepsilon_\theta^{(n-1)} + \Delta\varepsilon_\theta^{th,(n)} + \Delta\varepsilon_\theta^{sw,(n)}\right)$$
$$- \zeta_8\sigma_r^{(n-1)} - \zeta_9\sigma_\theta^{(n-1)},$$

$$\zeta_1 = \frac{g_{12} + 2g_{11} - 2g_{21}}{g_{11}} + \frac{r}{g_{11}}\frac{\partial g_{11}}{\partial r}, \quad \zeta_2 = \frac{g_{12} - 2g_{22}}{g_{11}} + \frac{r}{g_{11}}\frac{\partial g_{12}}{\partial r},$$

$$\zeta_3 = \frac{g_{12}}{g_{11}}, \quad \zeta_4 = \frac{b_{11}}{g_{11}}, \quad \zeta_5 = \frac{b_{12}}{g_{11}},$$

$$\zeta_6 = 2\frac{g_{11} - g_{21}}{g_{11}} + \frac{r}{g_{11}}\frac{\partial g_{11}}{\partial r}, \quad \zeta_7 = 2\frac{g_{12} - g_{22}}{g_{11}} + \frac{r}{g_{11}}\frac{\partial g_{12}}{\partial r},$$

$$\zeta_8 = 2\frac{b_{11} - b_{21}}{g_{11}} + \frac{r}{g_{11}}\frac{\partial b_{11}}{\partial r}, \quad \zeta_9 = 2\frac{b_{12} - b_{22}}{g_{11}} + \frac{r}{g_{11}}\frac{\partial b_{12}}{\partial r}.$$

Eq. (11) can be solved through a finite element method using the Galerkin form of the weighted residuals procedure [12]. In the finite element method, the shell is divided into several finite elements in the radial direction as shown in Fig. 3. Fig. 4 shows a two-node finite element and its shape functions expressed in a natural local coordinate system. A local system of the equations can be obtained by integrating
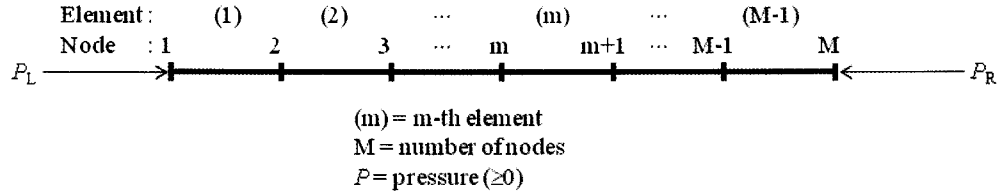
Element :   (1)   (2)   ⋯   (m)   ⋯   (M-1)

Node : 1   2   3   ⋯   m   m+1   ⋯   M-1   M

P_L ⟶ |————|————|——⋯——|————|——⋯——|————| ⟵ P_R

(m) = m-th element
M = number of nodes
P = pressure (≥0)

Fig. 3 Finite Element Divisions in a Single Layer

$N_1 = (1-\xi)/2$ $N_2 = (1+\xi)/2$

ξ : -1   1
r : r_- r_+

ξ = natural coordinate
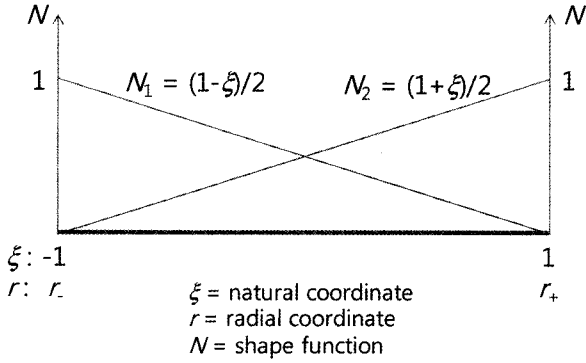r = radial coordinate
N = shape function

Fig. 4. Notation and Linear Shape Functions in a Natural Local Coordinate System

Eq. (11) over the interval in a finite element as shown in Fig. 4 through the weak formulation in Appendix B.

$$\begin{bmatrix} e_{11} & e_{12} \\ e_{21} & e_{22} \end{bmatrix} \begin{Bmatrix} u_1 \\ u_2 \end{Bmatrix} = \begin{Bmatrix} -4\pi r_-^2 \left(\dfrac{\partial u}{\partial r}\right)_{r_-} \\ 4\pi r_+^2 \left(\dfrac{\partial u}{\partial r}\right)_{r_+} \end{Bmatrix} + \begin{Bmatrix} f_1 \\ f_2 \end{Bmatrix}, \qquad (12)$$

where

$$e_{ij} = \sum_{k=1}^{2} 4\pi \omega_k \left[\frac{r_k^2}{J_k} N'_{i,k} N'_{j,k} + \left(2 - \zeta_{1,k}\right) r_k N_{i,k} N'_{j,k} - \zeta_{2,k} J_k N_{i,k} N_{j,k} \right], \quad (13)$$

$$f_i = -\sum_{k=1}^{2} 4\pi \omega_k r_k J_k \left(r_k \lambda_{1,k} + \lambda_{2,k} \right) N_{i,k}, \qquad (14)$$

$r_k = r(\xi_k)$, $J_k = J(\xi_k)$, $N_{i,k} = N_i(\xi_k)$, $N'_{i,k} = N'_i(\xi_k)$,

$\zeta_{m,k} = \zeta_m(\xi_k)$, $\lambda_{m,k} = \lambda_m(\xi_k)$,

$i = 1, 2, j = 1, 2$, and $m = 1, 2$.

The local equation, Eq. (12), should be assembled for all finite elements in a layer. Assembling Eq. (12) for all finite elements of a single layer in Fig. 3 gives the following equation.

$$\begin{bmatrix} e_{11}^{(1)} & e_{12}^{(1)} & 0 & 0 & 0 & \cdots & 0 \\ e_{21}^{(1)} & e_{22}^{(1)} + e_{11}^{(2)} & e_{12}^{(2)} & 0 & 0 & \cdots & 0 \\ 0 & e_{21}^{(2)} & e_{22}^{(2)} + e_{11}^{(3)} & e_{12}^{(3)} & 0 & \cdots & 0 \\ \vdots & \vdots & \vdots & \vdots & \vdots & & \vdots \\ 0 & 0 & \cdots & 0 & e_{21}^{(M-2)} & e_{22}^{(M-2)} + e_{11}^{(M-1)} & e_{12}^{(M-1)} \\ 0 & 0 & \cdots & 0 & 0 & e_{21}^{(M-1)} & e_{22}^{(M-1)} \end{bmatrix} \begin{Bmatrix} u_1 \\ u_2 \\ \vdots \\ u_M \end{Bmatrix}$$

$$= \begin{Bmatrix} f_1^{(1)} \\ f_2^{(1)} + f_1^{(2)} \\ \vdots \\ f_2^{(M-2)} + f_1^{(M-1)} \\ f_2^{(M-1)} \end{Bmatrix} + \begin{Bmatrix} -4\pi r_1^2 \left(\dfrac{\partial u}{\partial r}\right)_{r_1}^{(1)} \\ 4\pi r_2^2 \left(\dfrac{\partial u}{\partial r}\right)_{r_2}^{(1)} - 4\pi r_2^2 \left(\dfrac{\partial u}{\partial r}\right)_{r_2}^{(2)} \\ \vdots \\ 4\pi r_{M-1}^2 \left(\dfrac{\partial u}{\partial r}\right)_{r_{M-1}}^{(M-2)} - 4\pi r_{M-1}^2 \left(\dfrac{\partial u}{\partial r}\right)_{r_{M-1}}^{(M-1)} \\ 4\pi r_M^2 \left(\dfrac{\partial u}{\partial r}\right)_{r_M}^{(M-1)} \end{Bmatrix} \qquad (15)$$

In the second vector of the right-hand side of Eq. (15), the interior elements of the vector vanish because the two derivatives of displacement with respect to the radial coordinate are the same. The derivative of displacement with respect to the radial coordinate is given from Eq. (9).

$$\frac{\partial u}{\partial r} = -\frac{\zeta_3}{r} u + \frac{\sigma_r^{(n)}}{g_{11}} + \frac{f'}{4\pi r^2}, \qquad (16)$$

where

$$f' = 4\pi r^2 \left[\varepsilon_r^{(n-1)} + \Delta\varepsilon_r^{th,(n)} + \Delta\varepsilon_r^{sw,(n)} + \zeta_3 \left(\varepsilon_\theta^{(n-1)} + \Delta\varepsilon_\theta^{th,(n)} + \Delta\varepsilon_\theta^{sw,(n)} \right) - \zeta_4 \sigma_r^{(n-1)} - \zeta_5 \sigma_\theta^{(n-1)} \right].$$

The final form of a global finite element equation is

obtained by inserting Eq. (16) into the derivative terms at the nodal points 1 and M in Eq. (15) and replacing the radial stresses at the nodal point 1 and M with the pressures acting on the surfaces, respectively, i.e., $\sigma_{r,1} = -P_L$ and $\sigma_{r,M} = -P_R$.

$$[V]\{u\} = \{x\} + \{x_P\},\qquad(17)$$

where

$$[V] = \begin{bmatrix} e_{11}^{(1)} - 4\pi r_1 \zeta_{3,1} & e_{12}^{(1)} & 0 & 0 & 0 & \cdots & 0 \\ e_{21}^{(1)} & e_{22}^{(1)} + e_{11}^{(2)} & e_{12}^{(2)} & 0 & 0 & \cdots & 0 \\ 0 & e_{21}^{(2)} & e_{22}^{(2)} + e_{11}^{(3)} & e_{12}^{(3)} & 0 & \cdots & 0 \\ \vdots & \vdots & \vdots & \vdots & \vdots & \vdots & \vdots \\ 0 & 0 & \cdots & 0 & e_{21}^{(M-2)} & e_{22}^{(M-2)} + e_{11}^{(M-1)} & e_{12}^{(M-1)} \\ 0 & 0 & \cdots & 0 & 0 & e_{21}^{(M-1)} & e_{22}^{(M-1)} + 4\pi r_M \zeta_{3,M} \end{bmatrix},$$

$$\{u\}^T = \{u_1 \quad u_2 \quad \cdots \quad u_M\},$$

$$\{x\}^T = \{f_1^{(1)} - f_1' \quad f_2^{(1)} + f_1^{(2)} \quad f_2^{(2)} + f_1^{(3)} \quad \cdots \quad f_2^{(M-2)} + f_1^{(M-1)} \quad f_2^{(M-1)} + f_M'\},$$

$$\{x_P\}^T = \{\delta_1 P_L \quad 0 \quad \cdots \quad 0 \quad -\delta_M P_R\},$$

$$\delta_j = \frac{4\pi r_j^2}{g_{11,j}}.$$

The dimensions of matrix $[V]$ are $M \times M$, and the column vectors $\{u\}$, $\{x\}$, and $\{x_P\}$ each have $M \times 1$ dimensions.

Eq. (17) should be solved numerically because the matrix $[V]$ and the vectors $\{x\}$ and $\{x_P\}$ include the radial coordinates. The displacements can be obtained through the successive substitution method [13]. This method allows changing material properties in a layer according to an irradiation and radial position through Eqs. (13) and (14) and, even better, it does not have any variations with respect to an irradiation or radial position.

2.2 Multiple Spherical Layers

Fig. 5 shows the geometric finite element modeling for multiple spherical layers under pressures at the leftmost and rightmost surfaces. The fictitious springs between the layers are drawn in Fig. 5 to express the mechanical

interactions between the layers easily. In Fig. 5, two nodes connected with a fictitious spring always have the same radial coordinates and displacements.

$$u_{M(\ell)} = u_{M(\ell)+1}, \quad \ell = 1, 2, \cdots, L-1,\qquad(18)$$

where

$$M(\ell) = \sum_{k=1}^{\ell} M_k.\qquad(19)$$

Assembling Eq. (17) for all layers accomplishes the following equation for the multiple layers.

$$[S]\{u\} = \{h\} + \{y\},\qquad(20)$$

where

$$[S] = \begin{bmatrix} [V]^{(1)} & [0] & [0] & \cdots & [0] \\ [0] & [V]^{(2)} & [0] & \cdots & [0] \\ \vdots & \vdots & \vdots & \vdots & \vdots \\ [0] & [0] & \cdots & [0] & [V]^{(L)} \end{bmatrix}, \{u\} = \begin{Bmatrix} u_1 \\ u_2 \\ \vdots \\ u_{M(L)} \end{Bmatrix}, \{h\} = \begin{Bmatrix} \{x\}^{(1)} \\ \{x\}^{(2)} \\ \vdots \\ \{x\}^{(L)} \end{Bmatrix}, \{y\} = \begin{Bmatrix} \{w\}^{(1)} \\ \{w\}^{(2)} \\ \vdots \\ \{w\}^{(L)} \end{Bmatrix},$$

$$\{w\}^{(1)} = \begin{Bmatrix} \delta_1 P_L \\ 0 \\ \vdots \\ 0 \\ \delta_{M(1)} q_1 \end{Bmatrix}, \{w\}^{(\ell)} = \begin{Bmatrix} -\delta_{M(\ell-1)+1} q_{\ell-1} \\ 0 \\ \vdots \\ 0 \\ \delta_{M(\ell)} q_\ell \end{Bmatrix}, \ell = 2, \cdots, L-1, \{w\}^{(L)} = \begin{Bmatrix} -\delta_{M(L-1)+1} q_{L-1} \\ 0 \\ \vdots \\ 0 \\ -\delta_{M(L)} P_R \end{Bmatrix}.$$

The dimensions of matrix $[S]$ are $M(L) \times M(L)$, and the matrices $\{u\}$, $\{h\}$, and $\{y\}$ are $M(L) \times 1$ column vectors. In Eq. (20), the unknowns are the displacements $\{u\}$ and the interfacial radial pressures $\{q\}$. Eqs. (18) and (20) can
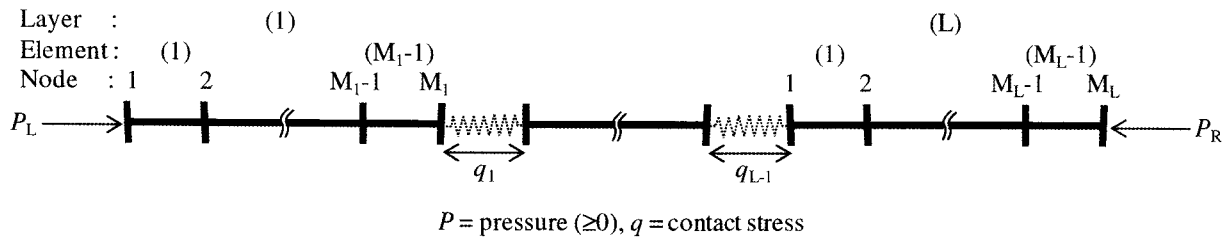

Fig. 5. Finite Element Divisions in Multiple Spherical Layers

be assembled and rearranged so that the unknowns appear in the left-hand side.

$$\begin{bmatrix} [S] & [Z'] \\ [Z] & [0] \end{bmatrix} \begin{Bmatrix} \{u\} \\ \{q\} \end{Bmatrix} = \begin{Bmatrix} \{h\} \\ \{0\} \end{Bmatrix} + \begin{Bmatrix} \{h'\} \\ \{0\} \end{Bmatrix},$$ (21)

where

$$[Z] = \begin{bmatrix} 0 & \cdots & 0 & 1 & -1 & 0 & & \cdots & & 0 \\ 0 & & \cdots & & 0 & 1 & -1 & 0 & \cdots & 0 \\ & & & & & & \ddots & & & \\ 0 & & \cdots & & & 0 & 1 & -1 & 0 & \cdots & 0 \end{bmatrix},$$

$$[Z'] = \begin{bmatrix} 0 & 0 & & 0 \\ \vdots & & & \\ 0 & & & \\ -\delta_{M(1)} & & & \\ \delta_{M(1)+1} & \vdots & & \vdots \\ 0 & & & \\ & 0 & & \\ & -\delta_{M(2)} & & \\ & \delta_{M(2)+1} & & \\ \vdots & 0 & & 0 \\ & & \ddots & -\delta_{M(L-1)} \\ & & & \delta_{M(L-1)+1} \\ \vdots & & & 0 \\ & & & \vdots \\ 0 & 0 & & 0 \end{bmatrix},$$

$$\{q\}^T = \{q_1 \quad q_2 \quad \cdots \quad q_{L-1}\}, \quad \{h'\}^T = \{\delta_1 P_L \quad 0 \quad \cdots \quad 0 \quad -\delta_{M(L)} P_R\}.$$

The dimensions of the matrices $[Z]$ and $[Z']$ are $(L-1) \times M(L)$ and $M(L) \times (L-1)$, respectively. The matrices $[Z]$ and $[Z']$ have the following elemental values, respectively.

$$z_{ij} = \begin{cases} 1 & \text{for } j = M(i), \ i = 1,2,\cdots,L-1 \\ -1 & \text{for } j = M(i)+1, \ i = 1,2,\cdots,L-1 \ , \\ 0 & \text{for others} \end{cases}$$

$$z'_{ij} = \begin{cases} -\delta_i & \text{for } i = M(j), \ j = 1,2,\cdots,L-1 \\ \delta_i & \text{for } i = M(j)+1, \ j = 1,2,\cdots,L-1 \ . \\ 0 & \text{for others} \end{cases}$$

Eq. (21) is very similar to the usual contact equation including the Lagrange multiplier [14]. The Lagrange multiplier means the contact force acting on an interface. The interfacial radial stress of Eq. (21) is equivalent to the

contact stress in the contact analysis. Eq. (21) is nonlinear for the displacements because the matrices $[S]$ and $[Z']$ and the vectors $\{h\}$ and $\{h'\}$ contain radial coordinates. The displacements and contact stresses can be solved through the successive substitution method as in the case of a single layer. The iteration is performed until the maximum relative error of displacements or contact stresses is less than or equal to a prescribed tolerance. The left-hand side of Eq. (21) is asymmetric and very sparse. LSLXG, a sparse linear solver of IMSL, or the Gauss-Jordan elimination method can be used to solve the asymmetric sparse system of equations [15,16]. For $\beta = 0$, the fluence increment in Eq. (21) is limited so that the creep strain increment should not exceed one-half of the total elastic strain for stable solutions [17]. For $\beta \geq 0.5$, the solution is unconditionally stable but there exists a fluence increment beyond which the solution becomes inaccurate. To be just on the accurate side, the fluence increment is controlled so that the creep strain increment is less than the total elastic strain [18].

Eq. (12) calculates the derivative of displacement with respect to the radial coordinate and Eq. (5) gives the total radial and tangential strains. Eq. (8) computes the stresses at the current fluence using the current strain increments and the previous stresses. Eq. (21) can be applied easily to any number of layers including a kernel without further manipulation of the solution procedure. Thus, we only need to change the number of layers. Eq. (21) is valid for a CFP in which all the layers bond to each other. If the layers separate from the other layers, a separate system of finite element equations like Eq. (21) should be set up for each separate system of the layers and the appropriate contact conditions should be applied to the separate layers.

2.3 Initial Conditions

The irradiation-induced dimensional change and creep strain of the coating layers are zeros at the initial step of irradiation. Applying Eqs. (1)-(6) to a CFP at the initial conditions gives the following second-order differential equation.

$$\frac{\partial^2 u}{\partial r^2} + \frac{\zeta_1^0}{r} \frac{\partial u}{\partial r} + \frac{\zeta_2^0}{r^2} u = \lambda_1^0 + \frac{\lambda_2^0}{r},$$ (22)

where

$$\zeta_1^0 = 2 + \frac{r}{d_{11}} \frac{\partial d_{11}}{\partial r}, \quad \zeta_2^0 = -2 + \frac{r}{d_{11}} \frac{\partial d_{12}}{\partial r},$$

$$\lambda_1^0 = \frac{\partial}{\partial r}\left(\varepsilon_r^{th} - \varepsilon_\theta^{th}\right) + \frac{1+v}{1-v}\frac{\partial \varepsilon_\theta^{th}}{\partial r}, \quad \lambda_2^0 = 2\frac{1-2v}{1-v}\left(\varepsilon_r^{th} - \varepsilon_\theta^{th}\right) + \frac{r}{d_{11}}\frac{\partial d_{11}}{\partial r}\varepsilon_r^{th} + \frac{r}{d_{11}}\frac{\partial d_{12}}{\partial r}\varepsilon_\theta^{th},$$

$$d_{11} = E\frac{1-v}{(1+v)(1-2v)}, \quad d_{12} = E\frac{2v}{(1+v)(1-2v)}.$$

Similarly with Section 2.1 and 2.2, a global finite element equation for the displacements and interfacial radial stresses is obtained.

3. CALCULATIONS AND DISCUSSIONS

The data of a CFP for test calculations were extracted from the IAEA CRP-6 benchmarking program for normal conditions [19]. Table 1-3 represents the extracted fabrication information, irradiation history, and material properties for a CFP [20]. Case B was selected to evaluate the effects of the cyclical pressure on the stresses of a CFP. Case C was chosen to calculate the failure fraction for the CFPs. Fig. 6 shows the internal pressures for Cases A and B. Fig. 7 displays the radial and tangential irradiation-induced dimensional changes of PyC for Cases A and B. The PyC shrinks with irradiation in the radial and tangential directions throughout the considered irradiation range.
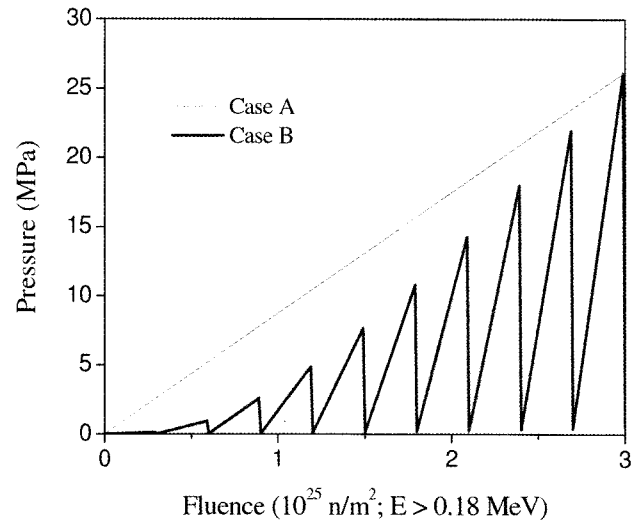

Fig. 6. Internal Pressures for Cases A and B

Table 1. Fabrication Data and Irradiation History for a Coated Fuel Particle

Parameters	Case A	Case B	Case C
Kernel diameter, μm	500	500	502±11
Buffer thickness, μm	100	100	95±14
IPyC thickness, μm	40	40	41±3
SiC thickness, μm	35	35	35±2
OPyC thickness, μm	40	40	40±4
Kernel density, g/cm³	10.8	10.8	10.81
Buffer density, g/cm³	0.95	0.95	1.01
IPyC density, g/cm³	1.9	1.9	1.87
SiC density, g/cm³	3.20	3.20	3.20
OPyC density, g/cm³	1.9	1.9	1.87
IPyC BAF[1]	1.03	1.03	1.02
OPyC BAF	1.03	1.03	1.02
Irradiation duration , EFPD[2]	1000	1000	600
End-of-life burnup, % FIMA[3]	10	10	20
End-of-life fluence, 10²⁵ n/m²; E>0.18 MeV	3	3	5.4
[4]Irradiation temperature, °C	1000	600 to 1000 (10 cycles)	1025
[5]End-of-life internal pressure, MPa	26.20	Table 2	73.11
Ambient pressure, MPa	0.1	0.1	0.1

[1] Bacon Anisotropy Factor
[2] Effective Full Power Days
[3] Fissions per Initial Metal Atoms
[4] For Cases A and C, temperature is constant through time and constant throughout the particle.
For Case B, temperature increases linearly from 600 to 1000 °C for each 100 day cycle and is constant throughout the particle.
[5] For Cases A and C, the internal gas pressure increases linearly with time from zero to the listed end-of-life value.

Table 2. Internal Pressure for Case B

Fast Fluence (10^{25}n/m²; E>0.18 MeV)	Irradiation Duration (EFPD)	Internal Pressure (MPa)
0.00	0.00	0.00
0.29	96.67	0.14
0.30	100.00	0.02
0.59	196.67	0.94
0.60	200.00	0.04
0.89	296.67	2.59
0.90	300.00	0.07
1.19	396.67	4.87
1.20	400.00	0.10
1.49	496.67	7.64
1.50	500.00	0.14
1.79	596.67	10.79
1.80	600.00	0.20
2.09	696.67	14.26
2.10	700.00	0.26
2.39	796.67	17.99
2.40	800.00	0.33
2.69	896.67	21.96
2.70	900.00	0.41
2.99	996.67	26.13
3.00	1000.00	0.50

Throughout the calculation, it is assumed that the thermal expansion of the coating layers occurs at a temperature higher than the deposition temperature of the coating layer, 1300 °C for PyC and 1500 °C for SiC [21].

The developed finite element method was implemented into the HTGR fuel performance analysis code, COPA, which is being developed at the Korea Atomic Energy Research Institute [22]. The stresses calculated by the present method were compared with those from a previously developed mechanical analysis code, STRESS3 [23]. Figs. 8 and 9 present the tangential stresses at the inner
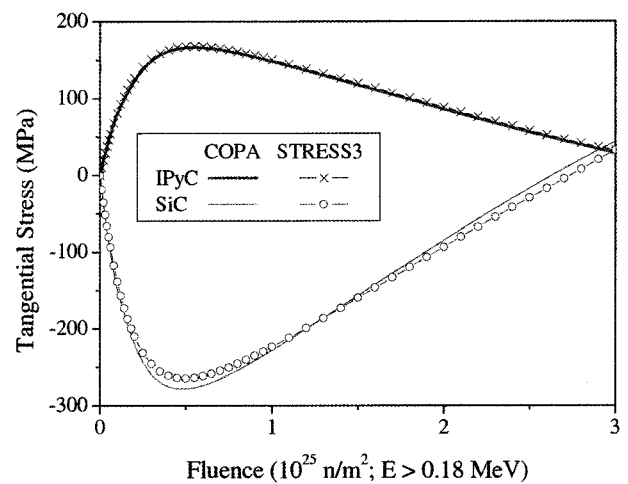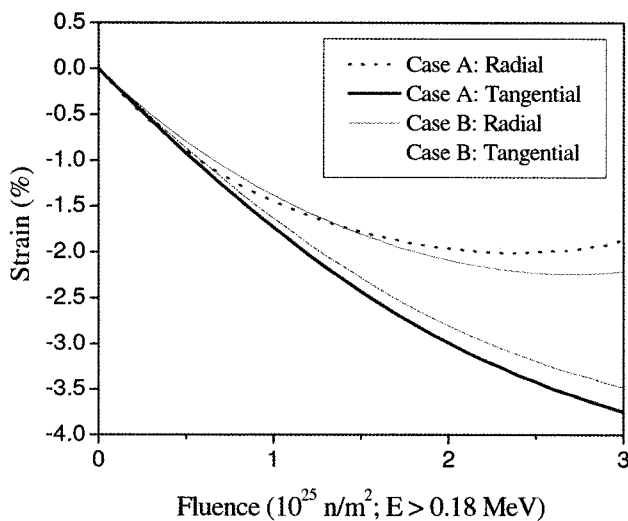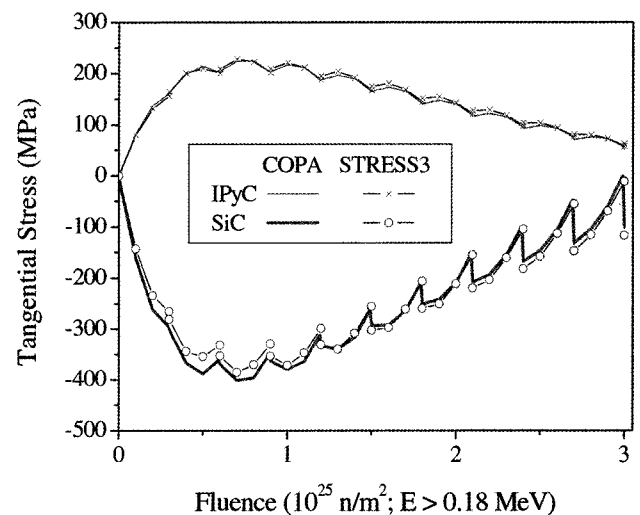

Fig. 8. Tangential Stresses at the Inner Surfaces of IPyC and SiC for Case A

Fig. 7. Radial and Tangential Irradiation-induced Dimensional Changes of PyC for Cases A and B

Fig. 9. Tangential Stresses at the Inner Surfaces of IPyC and SiC for Case B

Table 3. Material Properties of PyC and SiC

Material properties	PyC	SiC
Elasticity, MPa	3.96×10^4	3.7×10^5
Poisson's ratio	0.33	0.13
Irradiation creep coefficient, $[MPa \cdot (10^{25} n/m^2; E > 0.18\ MeV)]^{-1}$	Case A: 2.7×10^{-4} Case B: Correlation (a) Case C: 4.93×10^{-4}	
Poisson's ratio in creep	Case A: 0.5 Case B: 0.5 Case C: 0.4	
Irradiation-induced dimensional change rate, $[(\Delta L/L)/(10^{25} n/m^2; E > 0.18\ MeV)]$	Case A: Correlation (b) Case B: Correlation (c) Case C: Correlation (d)	
Thermal expansion coefficient, K^{-1}	5.50×10^{-6}	4.90×10^{-6}
Mean strength, MPa	200	873
Weibull modulus	5.0	8.02

Irradiation-induced dimensional change rate and irradiation creep coefficient

Correlation (a) : $K = 4.386 \times 10^{-4} - 9.70 \times 10^{-7}T + 8.0294 \times 10^{-10}T^2$

Correlation (b) :

$\dot{\varepsilon}_r^{sw} = 1.36334 \times 10^{-3} \phi^3 - 7.77024 \times 10^{-3} \phi^2 + 2.00861 \times 10^{-2} \phi - 2.22642 \times 10^{-2}$

$\dot{\varepsilon}_{\theta}^{sw} = -3.53804 \times 10^{-4} \phi^3 + 1.69251 \times 10^{-3} \phi^2 + 2.63307 \times 10^{-3} \phi - 1.91253 \times 10^{-2}$

Correlation (c) :

$\dot{\varepsilon}_r^{sw} = 4.03266 \times 10^{-4} \phi^3 - 2.25937 \times 10^{-3} \phi^2 + 9.82884 \times 10^{-3} \phi - 1.80613 \times 10^{-2}$

$\dot{\varepsilon}_{\theta}^{sw} = -4.91648 \times 10^{-4} \phi^3 + 2.32979 \times 10^{-3} \phi^2 + 1.71315 \times 10^{-3} \phi - 1.78392 \times 10^{-2}$

Correlation (d) :

$$\dot{\varepsilon}_r^{nr} = \begin{cases} 4.52013 \times 10^{-4} \phi^5 - 8.36313 \times 10^{-3} \phi^4 + 5.67549 \times 10^{-2} \phi^3 - 1.74247 \times 10^{-1} \phi^2 \\ +2.62692 \times 10^{-1} \phi - 1.43234 \times 10^{-1} \qquad \text{for } \phi \le 6.08 \\ \qquad\qquad 0.0954 \qquad\qquad\qquad\qquad \text{for } \phi > 6.08 \end{cases}$$

$$\dot{\varepsilon}_{\theta}^{nr} = \begin{cases} 1.30457 \times 10^{-4} \phi^3 - 2.10029 \times 10^{-3} \phi^2 + 9.07826 \times 10^{-3} \phi - 3.24737 \times 10^{-2} \quad \text{for } \phi \le 6.08 \\ \qquad\qquad -0.0249 \qquad\qquad\qquad\qquad\qquad\qquad \text{for } \phi > 6.08 \end{cases}$$

where

K = Irradiation creep coefficient, $[MPa \cdot (10^{25} n/m^2; E > 0.18\ MeV)]^{-1}$

$\dot{\varepsilon}_r^{sw}$ = Radial irradiation-induced dimensional change rate $[(\Delta L/L)/(10^{25} n/m^2; E > 0.18\ MeV)]$

$\dot{\varepsilon}_{\theta}^{sw}$ = Tangential irradiation-induced dimensional change rate $[(\Delta L/L)/(10^{25} n/m^2; E > 0.18\ MeV)]$

T = Temperature in °C.

ϕ = Fast fluence ($10^{25} n/m^2$; E > 0.18 MeV)

surfaces of the IPyC and SiC layers for Cases A and B which were calculated by COPA and STRESS3, respectively. In these cases, the number of finite elements in a coating layer was set to 4 and the number of coating layers to 3. Then the left-hand matrix of Eq. (21) has the dimensions of 17×17. The β factor was set to 0.5. Stress results from COPA and STRESS3 are in very good agreement in both cases. Fig. 9 shows the cyclic variations of the stresses according to the cyclic internal pressure. Fig. 10 displays the tangential stresses at the inner surfaces of the IPyC
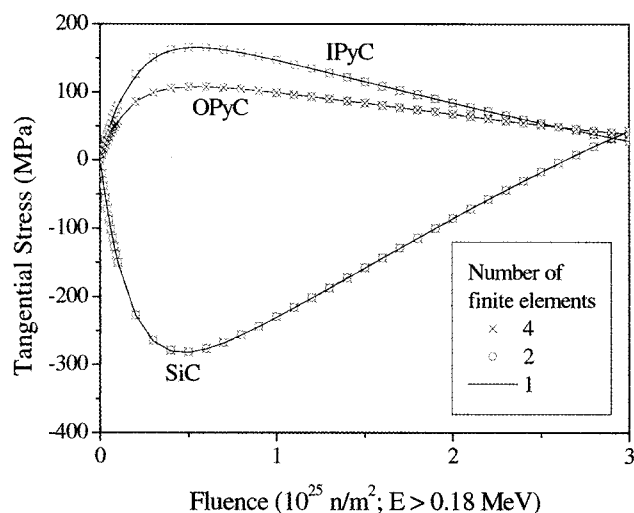
Fig. 10. Tangential Stresses at the Inner Surfaces of IPyC and SiC according to the Number of Finite Elements in Case A

Table 4. Failure Fractions and Computer Times for Case C

Number of Monte Carlo Runs	SiC Failure Fraction	[1]CPU Time, second
10^4	4.80×10^{-3}	84
10^5	5.14×10^{-3}	842
10^7	5.20×10^{-3}	83707

[1] A personal computer with Intel(R) Core(TM)2 Quad CPU of 2.66 GHz and 2 GB RAM was used.

and SiC layers for Case A according to the number of finite elements in a coating layer. The method produces accurate stresses even when the number of finite elements is one, the least number of finite elements. This means that a small number of finite elements are sufficient to calculate the failure probability of a batch of CFPs in the present method. Table 4 presents the computer time taken to calculate the failure fraction of the SiC layer due to only a pressure vessel failure mechanism for the CFPs of Case C using the COPA code. A quad core Pentium personal computer was used in the calculation. The number of finite elements in a coating layer was set to one. It takes about 23.3 hours to perform 10^7 Monte Carlo runs, where the minimum failure fraction is 1×10^{-7}. The present method is not practical for Monte Carlo runs of more than 10^7 using a quad core Pentium personal computer.

In Fig. 8 or 10, the tangential stress of the inner surface of IPyC rises to a high value at about 0.5×10^{25} n/m^2; $E > 0.18$ MeV and then subsequently decreases. Fig. 11 shows the tangential stresses at the inner surface of the IPyC layer according to the deformation behavior and the internal pressure at the early stage of irradiation. The inner surface of the IPyC shrinks in the positive radial direction due to irradiation. The shrinkage creates a tensile stress in the tangential direction at the inner surface of the IPyC. The irradiation-induced creep of the IPyC relieves the stress. The internal pressure does not greatly contribute to the stress generation in this early stage of irradiation because it is low. Fig. 12 sketches the tangential stresses of the inner surface of the SiC layer according to the deformation behavior and the internal pressure at the early stage of irradiation. The IPyC layer pulls the inner surface of the SiC layer when it shrinks under irradiation, which results in a compressive tangential
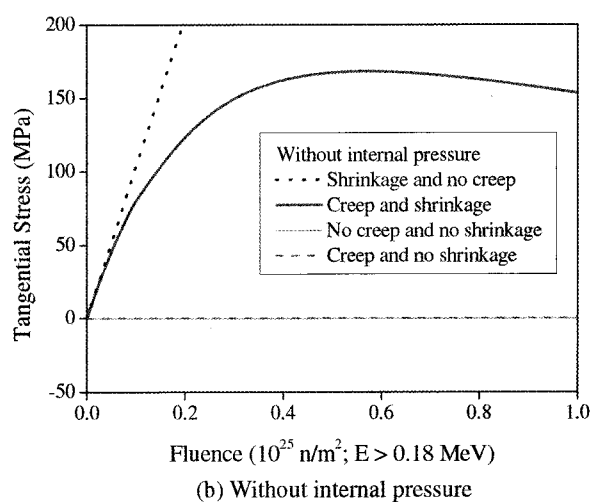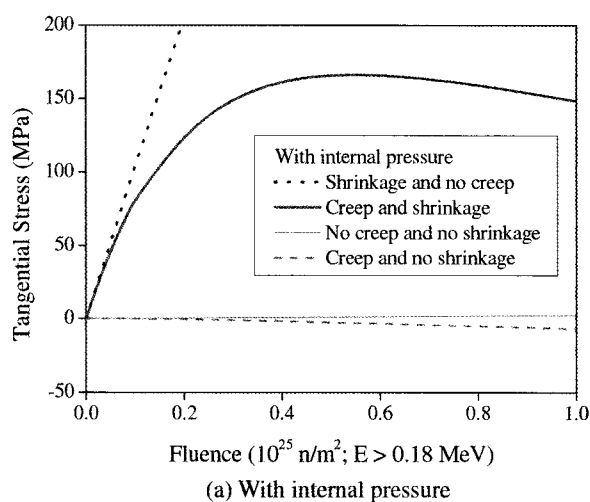

(a) With internal pressure

(b) Without internal pressure

Fig. 11. Tangential Stresses of IPyC Inner Surface according to Deformation Behavior and Internal Pressure in Case A

(a) With internal pressure
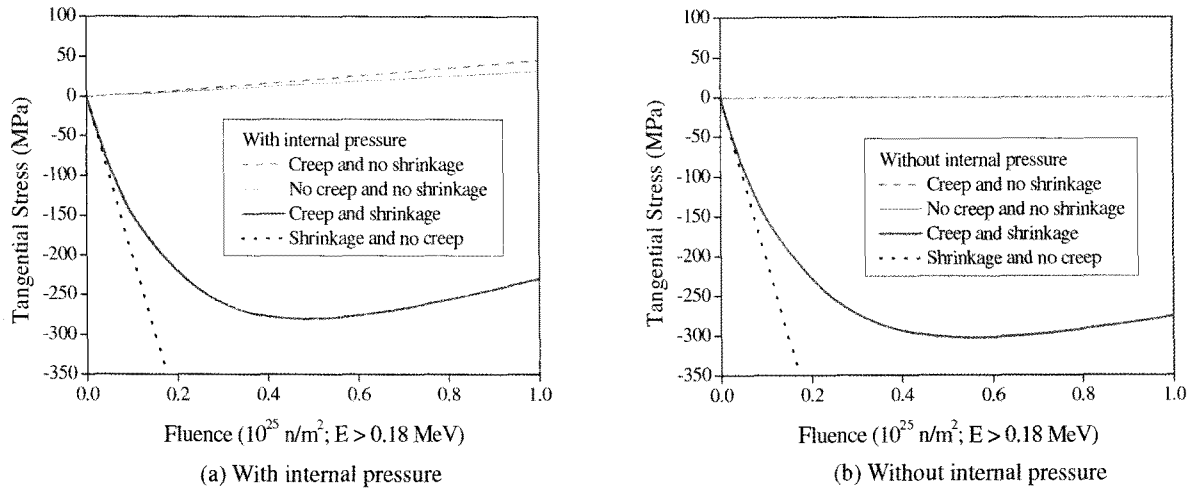
(b) Without internal pressure

Fig. 12. Tangential Stresses of SiC Inner Surface according to Deformation Behavior and Internal Pressure in Case A
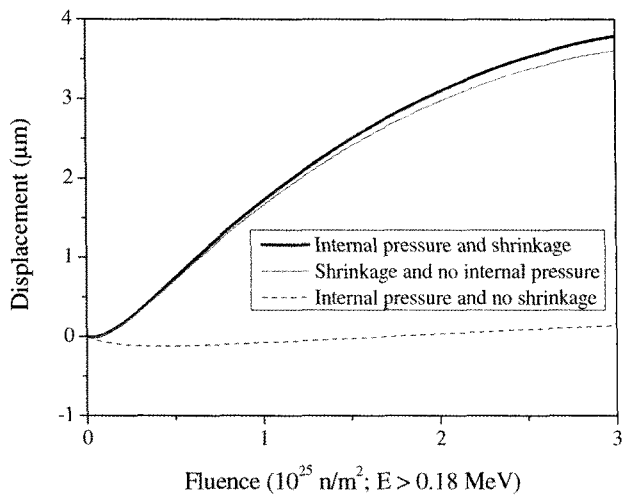

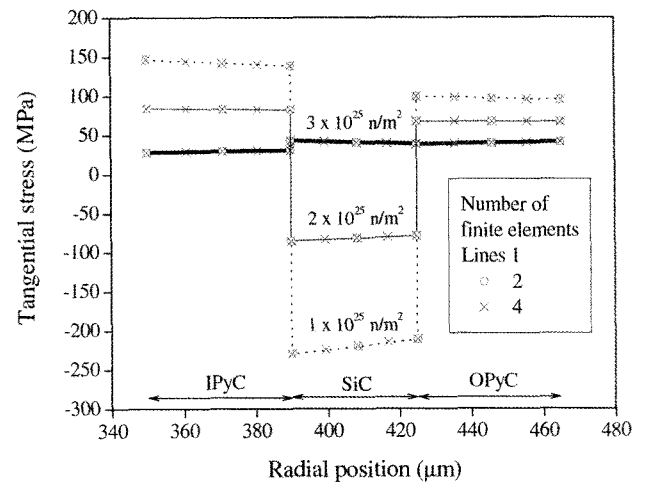Fig. 13. Radial Displacements of the Inner Surface of the IPyC in Case A

Fig. 14. Variations of Tangential Stresses along the Radial Position according to the Number of Finite Elements in Case A

stress for the inner surface of SiC. The irradiation-induced creep of the IPyC relieves the stress acting on the SiC too. Fig. 13 illustrates the radial displacements of the inner surfaces of the IPyC according to the internal gas pressure and the irradiation-induced shrinkage. The irradiation-induced shrinkage of the IPyC generates most of the radial displacement of the IPyC inner surface throughout the irradiation. Fig. 14 shows the tangential stresses along the radial position according to the number of finite elements. The number of finite elements does not affect the calculated results of tangential stresses

along the radial coordinate. Maximum stresses occur at the inner surfaces for all the layers.

4. CONCLUSIONS

A numerical method has been developed to perform mechanical analyses for a CFP of a HTGR using a finite element method. The solution procedure is very simple and can be easily applied to the stress analysis for any design of a CFP. Material properties in the layers of a

CFP can be changed easily according to the time and radial position. The stresses calculated by the finite element method agreed well with the results from a previously developed computer code. The irradiation-induced dimensional change produces considerable stresses on the coating layers and the irradiation-induced creep relieves the stresses. The developed finite element method generates accurate results even when the number of finite elements is one, which means that a small number of finite elements can be set to calculate the failure probability of CFPs. The more improved finite element method will include a contact analysis scheme which will make it possible to analyze the mechanical behavior of separate layers in a CFP.

APPENDIX A

The elements of the matrices [G] and [B]

$$g_{11} = \frac{1}{X}\left[\frac{1-\nu^{(n)}}{E^{(n)}} + \beta\Delta\phi^{(n)} K^{(n)}\left(1-\mu^{(n)}\right)\right], \quad g_{12} = \frac{2}{X}\left(\frac{\nu^{(n)}}{E^{(n)}} + \beta\Delta\phi^{(n)} K^{(n)}\mu^{(n)}\right),$$

$$g_{21} = \frac{1}{X}\left(\frac{\nu^{(n)}}{E^{(n)}} + \beta\Delta\phi^{(n)} K^{(n)}\mu^{(n)}\right), \quad g_{22} = \frac{1}{X}\left(\frac{1}{E^{(n)}} + \beta\Delta\phi^{(n)} K^{(n)}\right),$$

where

$$X = \left(\frac{1}{E^{(n)}} + \beta\Delta\phi^{(n)} K^{(n)}\right)\left[\frac{1-\nu^{(n)}}{E^{(n)}} + \beta\Delta\phi^{(n)} K^{(n)}\left(1-\mu^{(n)}\right)\right] - 2\left(\frac{\nu^{(n)}}{E^{(n)}} + \beta\Delta\phi^{(n)} K^{(n)}\mu^{(n)}\right)^2.$$

$$b_{11} = g_{11}\left[\frac{1}{E^{(n-1)}} - (1-\beta)\Delta\phi^{(n)} K^{(n-1)}\right] + g_{12}\left[-\frac{\nu^{(n-1)}}{E^{(n-1)}} + (1-\beta)\Delta\phi^{(n)} K^{(n-1)}\mu^{(n-1)}\right],$$

$$b_{12} = 2g_{11}\left[-\frac{\nu^{(n-1)}}{E^{(n-1)}} + (1-\beta)\Delta\phi^{(n)} K^{(n-1)}\mu^{(n-1)}\right] + g_{12}\left[\frac{1-\nu^{(n-1)}}{E^{(n-1)}} - (1-\beta)\Delta\phi^{(n)} K^{(n-1)}\left(1-\mu^{(n-1)}\right)\right],$$

$$b_{21} = g_{21}\left[\frac{1}{E^{(n-1)}} - (1-\beta)\Delta\phi^{(n)} K^{(n-1)}\right] + g_{22}\left[-\frac{\nu^{(n-1)}}{E^{(n-1)}} + (1-\beta)\Delta\phi^{(n)} K^{(n-1)}\mu^{(n-1)}\right],$$

$$b_{22} = 2g_{21}\left[-\frac{\nu^{(n-1)}}{E^{(n-1)}} + (1-\beta)\Delta\phi^{(n)} K^{(n-1)}\mu^{(n-1)}\right] + g_{22}\left[\frac{1-\nu^{(n-1)}}{E^{(n-1)}} - (1-\beta)\Delta\phi^{(n)} K^{(n-1)}\left(1-\mu^{(n-1)}\right)\right].$$

APPENDIX B

Weak formulation of Eq. (11) through the Galerkin method

When the solution of Eq. (11) is approximated, the integral of the weighted residual vanishes over a finite element interval.

$$\int_\Omega \Psi\left(\frac{\partial^2 u}{\partial r^2} + \frac{\zeta_1}{r}\frac{\partial u}{\partial r} + \frac{\zeta_2}{r^2}u - \lambda_1 - \frac{\lambda_2}{r}\right)d\Omega = 0. \qquad (B.1)$$

For a spherical finite element like Fig. 4, Eq. (B.1) becomes

$$\int_{r_-}^{r_+} \Psi\left(\frac{\partial^2 u}{\partial r^2} + \frac{\zeta_1}{r}\frac{\partial u}{\partial r} + \frac{\zeta_2}{r^2}u\right)4\pi r^2 dr = \int_{r_-}^{r_+} \Psi\left(\lambda_1 + \frac{\lambda_2}{r}\right)4\pi r^2 dr. \qquad (B.2)$$

In Eq. (B.2), the integrand including the second partial derivative of displacement with respect to radial coordinate can be transformed into the following equation by partial integration.

$$\int_{r_-}^{r_+} 4\pi r^2 \Psi\frac{\partial^2 u}{\partial r^2}dr = \left[4\pi r^2\Psi\frac{\partial u}{\partial r}\right]_{r_-}^{r_+} - \int_{r_-}^{r_+}\left(4\pi r^2\frac{\partial\Psi}{\partial r} + 8\pi r\Psi\right)\frac{\partial u}{\partial r}dr. \qquad (B.3)$$

Inserting Eq. (B.3) into Eq. (B.2) gives Eq. (B.4).

$$\int_{r_-}^{r_+} 4\pi\left[r^2\frac{\partial\Psi}{\partial r}\frac{\partial u}{\partial r} + (2-\zeta_1)r\Psi\frac{\partial u}{\partial r} - \zeta_2\Psi u\right]dr$$

$$= \left[4\pi r^2\Psi\frac{\partial u}{\partial r}\right]_{r_-}^{r_+} - \int_{r_-}^{r_+}\Psi(r\lambda_1 + \lambda_2)4\pi r\,dr \qquad (B.4)$$

In the Galerkin method, the weighting function is set equal to the shape function.

$$\Psi = N_i, \qquad (B.5)$$

where i is a node number in a finite element. The approximated displacement can be expressed in the summation of the product of shape function and displacement at nodes.

$$u = \sum_j N_j u_j, \qquad (B.6)$$

where j is a node number in a finite element. In natural coordinate system, Eq. (B.4) becomes

$$\int_{-1}^{1} 4\pi\left[\frac{r^2}{J}N_i'\sum_j N_j'u_j + (2-\zeta_1)rN_i\sum_j N_j'u_j - \zeta_2 JN_i\sum_j N_j u_j\right]d\xi$$

$$= -4\pi r_-^2 N_i(-1)\left(\frac{\partial u}{\partial r}\right)_{r_-} + 4\pi r_+^2 N_i(1)\left(\frac{\partial u}{\partial r}\right)_{r_+} - \int_{-1}^{1}4\pi rJ(r\lambda_1 + \lambda_2)N_i\,d\xi \qquad (B.7)$$

NOMENCLATURE

r	Radial coordinate (m)
r_L	Radial coordinate of the leftmost surface (m)
r_R	Radial coordinate of the rightmost surface (m)
r_-	Radial coordinate of the leftmost node in a finite element (m)
r_+	Radial coordinate of the rightmost node in a finite element (m)
u	Radial displacement (m)
E	Young's modulus (MPa)
K	Irradiation creep coefficient [MPa$\cdot(10^{25}$ n/m^2; E > 0.18 MeV)]$^{-1}$
J	Jacobian $= \dfrac{dr}{d\xi}$,
L	Number of layers,
M	Number of nodes in a single layer $= M_l$,
M_k	Number of nodes in layer k
$M(l)$	Global node number of the last node of layer l, $M(0) = 0$
N	Shape function
P_L	Pressure acting on the leftmost surface ≥ 0 (MPa)
P_R	Pressure acting on the rightmost surface ≥ 0 (MPa)
q	Interfacial radial stress between two adjacent coating layers (MPa)
T	Irradiation temperature (K)
T_{dep}	Deposition temperature of a coating layer (K)

Greek Symbols

α	Thermal expansion coefficient (K^{-1})
ε	Total strain
ε^{cr}	Irradiation-induced creep strain
ε^{sw}	Irradiation-induced dimensional change
ε^{th}	Thermal strain $= \alpha(T\text{-}T_{dep})$
μ	Poisson's ratio in irradiation creep
ν	Poisson's ratio
ξ	Natural coordinate
σ	Stress (MPa)
ϕ	Fast neutron fluence (10^{25} n/m^2; E > 0.18 MeV)
ω_k	Weight of an integration point k
Ψ	Weighting function
Ω	Volume of a finite element (m^3)

Superscripts

(n)	n-th fluence step
(l)	l-th layer

Subscripts

r	Radial direction
θ	Tangential direction

ACKNOWLEDGMENTS

REFERENCES

[1] J. W. Prados and J. L. Scott, "Mathematical Model for Predicting Coated-Particle Behavior," *Nucl. Appl.*, **2**, 402 (1966).

[2] J. L. Kaae, "A Mathematical Model for Calculating Stresses in a Four-layer Carbon-Silicon-Carbide-Coated Fuel Particle," *J. Nucl. Mater.*, **32**, 322 (1969).

[3] H. Walther, "On Mathematical Models for Calculating the Mechanical Behaviour of Coated Fuel Particles," *Nucl. Eng. Des.*, **18**, 11 (1972).

[4] D. G. Martin, "An Analytical Method of Calculating, to a Reasonable Accuracy, Stresses in the Coatings of HTR Fuel Particles," *J. Nucl. Mater.*, **44**, 35 (1973).

[5] G. K. Miller, D. A. Petti, J. T. Maki, and D. L. Knudson, "Updated Solution for Stresses and Displacements in TRISO-coated Fuel Particles," *J. Nucl. Mater.*, **374**, 129 (2008).

[6] R. G. Bennet, "Finite Element Stress Analysis for Coated Particle Fuel Modeling under Normal Operating Conditions," *Nucl. Technol.*, **96**, 117 (1991).

[7] G. K. Miller, D. A. Petti, D. J. Varacalle Jr., and J. T. Maki, "Statistical Approach and Benchmarking for Modeling of Multi-Dimensional Behavior in TRISO-Coated Fuel Particles," *J. Nucl. Mater.*, **317**, 69 (2003).

[8] G. K. Miller, D. A. Petti, and J. T. Maki, "Consideration of the Effects of Partial Debonding of the IPyC and Particle Asphericity on TRISO-Coated Fuel Behavior," *J. Nucl. Mater.*, **334**, 79 (2004).

[9] T. D. Gulden, C. L. Smith, and D. P. Harmon, "The Mechanical Design of TRISO-coated Particle Fuels for the Large HTGR," *Nucl. Technol.*, **16**, 100 (1972).

[10] J. L. Kaae, "On Irradiation-Induced Creep of Pyrolytic Carbon in a General State of Stress," *J. Nucl. Mater.*, **34**, 206 (1970).

[11] S. P. Timoshenko, and J. N. Goodier, *Theory of Elasticity*, 3rd ed., McGraw-Hill, Inc. (1970).

[12] D. W. Pepper and Juan C. Heinrich, *The Finite Element Method*, Hemisphere Publishing Corporation, USA (1992).

[13] F. B. Hildebrand, *Introduction to Numerical Analysis, 2nd ed.*, Dover Publications, Inc. (1987).

[14] R. D. Cook, D. S. Malkus, and M. E. Plesha, *Concepts and Applications of Finite Element Analysis, 3rd ed.*, John Wiley & Sons, Inc. (1981).

[15] *IMSL Fortran Numerical Library, version 5.0: IMSL MATH/LIBRARY Volume 1*, Visual Numerics, Inc. (2003).

[16] W. H. Press, S. A. Teukolsky, W. T. Vetterling, and B. P. Flannery, *Numerical Recipes in FORTRAN, 2nd ed.*, Cambridge University Press (1992).

[17] O. C. Zienkiewicz, *The Finite Element Method, third ed.*, McGraw-Hill Book Company (UK) Limited (1977).

[18] G. A. Greenbaum, "Creep Analysis of Axisymmetric Bodies using Finite Elements," *Nucl. Eng. Des.*, **7**, 379 (1968).

[19] K. Verfondern and Y. W. LEE, "Advances in HTGR Fuel Technology - A New IAEA Coordinated Research Program," *2005 International Congress on Advances in Nuclear Power Plants (ICAPP05)*, May 15 - 19, 2005, Seoul, Korea.

[20] J. T. Maki and G. K. Miller, "TRISO-Coated Particle Fuel Performance Benchmark Cases," unnumbered document (2005).

[21] D. A. Petti, J. T. Maki, J. Buongiorno, R. R. Hobbins, and G. K. Miller, *Key Differences in the Fabrication, Irradiation and Safety Testing of U.S. and German TRISO-coated Particle Fuel and Their Implications on Fuel Performance*, INEEL/EXT-02-00300 (2002).

[22] Y. M. Kim, M. S. Cho, Y. W. Lee, and W. J. Lee, "Development of a Fuel Performance Analysis Code COPA," *Proceedings of the 4th International Topical Meeting on High Temperature Reactor Technology (HTR-2008),* September 28 - October 1, 2008, Washington D.C., USA.

[23] D. G. Martin, "A UK contribution to the CRP6 benchmarking of fuel performance codes during normal operation. Part 2: Cases 5-8," CRP6/DGM/05/01 (2005).